Document Version
Final published version

Citation (APA)
Anju, R. S., Kumar, P., Naikwadi, D. R., Konings, M. C., Stam, P. G., Ariese, F., Baumgartner, B., Bansode, A., Shiju, N. R., & More Authors (2026). Beyond metals: Tailored metal-free boron-oxy-carbide catalysts for CO2 hydrogenation. *Applied Catalysis B: Environmental*, *384*, Article 126153. https://doi.org/10.1016/j.apcatb.2025.126153

Applied Catalysis B: Environment and Energy 384 (2026) 126153

Contents lists available at ScienceDirect

Applied Catalysis B: Environment and Energy

journal homepage: www.elsevier.com/locate/apcatb

Beyond metals: Tailored metal-free boron-oxy-carbide catalysts for CO_2 hydrogenation

Rajamohanan Sobhana Anju [a], Pankaj Kumar [b], Dhanaji R. Naikwadi [c], Merel C. Konings [d], Pascal G. Stam [a], Freek Ariese [d], Bettina Baumgartner [e], Atul Bansode [c], Fengshou Yu [f], Erdni D. Batyrev [g], Paula Oulego [h], Vimal Chandra Srivastava [b], N. Raveendran Shiju [a,*]

[a] Catalysis Engineering Group, Van 't Hoff Institute for Molecular Sciences, University of Amsterdam, Science Park 904, 1090GD Amsterdam, The Netherlands
[b] Department of Chemical Engineering, Indian Institute of Technology Roorkee, Roorkee, India
[c] Department of Chemical Engineering, Delft University of Technology, Van der Massweg 9, 2629 Hz Delft, the Netherlands
[d] LaserLaB, Department of Physics and Astronomy, Vrije Universiteit Amsterdam, Amsterdam, The Netherlands
[e] Homogeneous, Supramolecular and Bio-Inspired Catalysis group, Van't Hoff Institute for Molecular Sciences, University of Amsterdam, Amsterdam, The Netherlands
[f] School of Chemical Engineering and Technology, Hebei University of Technology, Tianjin, China
[g] Tata Steel Research & Development; IJmuiden, The Netherlands
[h] Department of Chemical and Environmental Engineering, University of Oviedo, Spain

ARTICLE INFO

Keywords:
Boron oxy carbide
Reverse Water Gas Shift Reaction
CO_2 hydrogenation
Metal-free catalysts
Borophene
Boron nanosheets

ABSTRACT

The rational design of functional materials through targeted element-selection strategies offers a promising route for developing next-generation catalysts. Here, we employ this strategy to tackle critical challenges in the Reverse Water Gas Shift (RWGS) reaction, including catalyst deactivation, low CO selectivity, and the high cost of conventional transition-metal catalysts. Through this approach, we designed and synthesized a novel class of metal-free boron-oxy-carbide (BO) catalysts. The catalyst exhibited 100 % CO selectivity and maintained equilibrium CO_2 conversion without deactivation for over 250 h at 600 °C. Advanced characterization techniques, combined with density functional theory (DFT) calculations suggested that the 'B-O-C triad' within the BO lattice is responsible for the RWGS activity. These findings demonstrate the potential of BO catalysts as robust, scalable, and sustainable alternatives to state-of-the-art transition-metal-based catalysts for CO_2 valorization. We anticipate that these findings will provide a foundation for the design and activity of metal-free catalysts applicable to a diverse range of chemical transformations.

1. Introduction

Designing efficient metal-free heterogeneous catalysts demands an integrated understanding of surface chemistry, electronic structure, reaction thermodynamics, stability, and selectivity. We employed a rational element-selection strategy to tailor catalyst composition for the Reverse Water-Gas Shift (RWGS) reaction, due to the scarcity of data on metal-free RWGS catalysts that limited traditional machine learning approaches [1]. RWGS catalysts typically consist of active metals or metal oxides supported on carriers [2,3]. While noble metals offer excellent hydrogenation activity, their high cost and limited availability hinder industrial use [4]. Alternatives like Cu, Ni, and Fe are more affordable but suffer from issues such as poor CO selectivity and metal particle aggregation leading to catalyst deactivation [5]. These issues severely limit their long-term operational stability, scalability, and economic viability for industrial CO_2 valorization. Additionally, vulnerability to gas poisoning and adverse environmental impacts associated with metals are at odds with the objectives of sustainability and renewability. Therefore, the goal is to develop stable metal-free catalysts by incorporating key components that enhance catalytic activity and CO selectivity while ensuring high stability.

For this, we identified boron as the core element of the catalyst lattice for its unconventional bonding behavior, electron deficiency, and strong Lewis acidity. All these properties are crucial for CO_2 adsorption and activation in RWGS reaction. To support these properties in a stable framework, we chose boron nano-sheets as the foundation of the catalyst design [6]. The intrinsic metallic character, polymorphism and high CO_2 adsorption efficiency of boron nano sheets further qualified it as a base

---

* Corresponding author.
E-mail address: n.r.shiju@uva.nl (N.R. Shiju).

https://doi.org/10.1016/j.apcatb.2025.126153
Received 30 September 2025; Received in revised form 29 October 2025; Accepted 3 November 2025

material for RWGS catalyst [7–9]. Furthermore, we planned to introduce carbon to the boron nano sheets, as carbon doping can enhance the lattice stability and generate charge-deficient boron sites (adjacent to carbon), to promote the catalytic activity [10]. Additionally, tuning the degree of oxidation in the boron sheet is believed to impact its catalytic efficiency by promoting CO_2 dissociation. Finally, to ensure CO selectivity, suppressing further hydrogenation to methane, we decided to include an alkali metal (potassium in our case) on the lattice [11,12]. With this hypothesis, we attempted to synthesize and investigate the potential of doped boron sheets in catalyzing the RWGS reaction.

Herein, we report an effective and cost-efficient strategy for the synthesis of stable free-standing derivatives of boron nanosheets achieving good yields. Additionally, for the first time, we demonstrate their application as catalysts in the RWGS reaction. The synthesis involves stepwise heating of borohydride precursors, (ABH_4; A = Na, K) to 600 °C in the presence of potassium /sodium salt of formate in different ratios. In 2020, Tai et al. showed that reduced two-dimensional boron sheets (BH) can be prepared by heating $NaBH_4$ in a hydrogen rich environment [13]. Inspired by this, we investigated the preparation of boron nanosheets using $NaBH_4$ and HCOOK as precursors, hypothesizing that HCOOK would act as an in situ hydrogen donor thereby eliminating the need for costly H_2 gas and providing a safer, more economical reducing atmosphere [14–17]. We further anticipated that the process would yield a lattice modified by carbon and potassium; which was certainly chosen for the increased efficiency of the RWGS catalyst [10–12].

2. Experimental section

2.1. Chemicals and reagents

Sodium borohydride (≥ 98 %), Potassium formate (99 %), and sodium formate (≥ 99 %), used for the synthesis were purchased from Merck. Potassium borohydride (98 %) was purchased from Thermo Scientific Chemicals. All the chemicals were used as received without further purification.

2.2. Synthesis of boron nanosheet derivatives (BHs and BOs)

To synthesise BHs, ABH_4 (A = Na, K) was thoroughly mixed with HCOOA (A = Na, K) using mortar and pestle in molar ratios 3:1 or 2:1. Subsequently, the resulting mixture was transferred to a quartz boat and placed in a tubular furnace. Further, the mixture was subjected to heating, to 600 °C under a nitrogen flow of 50 mL/minute; following the heating profile illustrated in Scheme S1a. Upon cooling, the resultant material was cautiously exposed to air and allowed to remain under atmospheric conditions for a duration of 3–4 h. During this time, alkali metals/alkali metal clusters formed during the reaction developed a tarnished appearance due to the formation of an oxide or hydroxide layer. Subsequently, the material was finely ground and subjected to sonication for 10 min after the addition of 30 mL of water. This addition was executed gradually, to prevent any vigorous reactions. The mixture was filtered and washed three times each with cold water and hot water to remove any oxalate or carbonate salts that may have formed, followed by drying in an oven at 120 °C for 3 h. The possible chemical reactions are shown in Scheme S1a and equations (1−3), see supporting information).

For the preparation of oxidised boron nanosheets (BO), ABH_4 and HCOOA were combined in a 1:1 molar ratio and treated under identical synthesis and work-up conditions (Scheme S1b and Equations (4−8), see supporting information). The active species (B-O-C) is formed when the BOs (BO_KK and BO_NaK) are heated to 450 °C under inert conditions.

2.3. Characterization

The XRD measurements were performed at TU Delft to determine the atomic arrangement in crystalline or amorphous materials by analysing the diffraction pattern of X-rays. A Bruker D8 Advance-ECO with Bragg-Brentano geometry was used, with CuKα_1 and Kα_2 radiation as the X-ray source. The XPS measurements were performed at Tata Steel IJmuiden, The Netherlands. Al-monochromated X-ray source was used at 15 mA and 15 kV to generate the X-ray photons and the emitted photoelectrons were collected from an area of 0.7 × 0.3 mm^2. The acquired XPS spectra were processed in CASA XPS software to determine the surface composition. TEM images were recorded at TU Delft on TEM JEOL11400 plus machine. Images were captured using a 4 K camera after fine-tuning the optics. HR-TEM images are recorded either on a JEM 2100 F or FEI Tecnai F30 microscope, operating at an accelerating voltage of 200 kV. The FEI Tecnai F30 microscope is equipped with a field emission gun (FEG) and a SuperTwin® objective lens, allowing a point-to-point resolution of 0.19 nm. The samples were prepared by dispersing the material in ethanol, followed by sonication and deposition onto carbon-coated copper grids, which were then air-dried. STEM-EDS measurements were recorded on a Titan aberration-corrected Transmission Electron Microscope. Samples were prepared by dispersing the materials in isopropyl alcohol, followed by deposition onto carbon-coated copper grids, which were then air-dried. Atomic Force Microscopy (AFM) was performed at TU Delft on an NT-MDT Ntegra Aura AFM system in semi contact mode using Nano sensors PPP-NCHR cantilevers with a resonance frequency of 350 kHz, with only a linear line-by-line flattening applied for post-processing; or with Bruker Dimension Icon from School of Chemical Engineering and Technology, Hebei University of Technology, Tianjin, China. Transmission infrared (IR) spectra were recorded at University of Amsterdam, using an Invenio R Fourier-transform infrared (FTIR) spectrometer (Bruker Optics, Ettlingen, Germany) equipped with a DLa-TGS detector. Spectra were collected in the range of 4000–600 cm^{-1} with a resolution of 4 cm^{-1}. For all measurements, KBr pellets were prepared with a total mass of 100 mg, containing 1 wt% of the sample. In-situ Diffuse Reflectance Infrared Fourier Transform Spectroscopy (DRIFTS) was carried out at TU Delft on a Nicolet 8700 spectrometer (Thermo Scientific) equipped with a TRS-detector (LN-MCT) and a high-temperature DRIFT cell with CaF_2 windows (HVC Praying Mantis, Harrick). The catalyst was diluted with neutral alumina to optimize the detector signal, and sample spectra were recorded by accumulating 128 scans at a resolution of 4 cm^{-1} under different gas flows, including helium for purging/flushing. CO_2 Temperature-Programmed Desorption (CO_2-TPD) experiments were carried out using a Micromeritics AutoChem II 2920 apparatus. Initially, the sample was pretreated under a helium flow (25 mL/min) at 140 °C for 30 min to remove moisture. Then, CO_2 adsorption was carried out at 30 °C for 90 min under a 10 % CO_2 (30 mL/min) until saturation. Afterwards, physisorbed CO_2 was removed by flushing with helium (25 mL/min) for 30 min. Finally, a TPD ramp was applied up to 700 °C at 5 °C/min under helium to monitor the desorption process. H_2 Temperature Programmed Desorption (H_2-TPD) experiments were performed with the help of the Micromeritics Autochem II 2920 apparatus. Initially, the sample was pretreated under argon flow (25 mL/min) at 140 °C for 30 min to remove moisture. Then, H_2 adsorption was carried out at 150 °C for 60 min under a pure H_2 flow (30 mL/min) until saturation. Afterwards, physisorbed H_2 was removed by purging with argon (25 mL/min) for 30 min. Finally, a TPD ramp was applied up to 700 °C at 5 °C/min under argon to monitor the desorption process. ICP measurement was performed on a ICP-OES Shimadzu ICPE-9820 plasma atomic emission spectrometer with a mini torch peristaltic pump (radio frequency power 1.2 KW, plasma gas 8 L/min, auxillary gas 0.6 L/min, carrier gas 0.7 L/min). Raman measurements were performed at Vrije Universiteit Amsterdam with an InVia Reflex Renishaw system. A frequency doubled Nd:YAG laser of 532 nm with a grating of 1200 l/mm was used (range between 450 and 2975 cm^{-1} or between 100 and 2715 cm^{-1}). The system is operated with Renishaw WIRE™ software. Particles of interest were measured with a 50x objective, with an exposure time of 1 s, accumulations between 10 and 20 and varying laser power of between 5 % and 10 % (depending on the intensity of the signal). The spectra were slightly smoothed, background-corrected, and normalized using MATLAB (version R2024a, 24.1.0.2603908). Smoothing was performed using the 'Smooth Data' task with a Savitzky-Golay polynomial filter, applying a moving window with a centre value of 5. Background correction was achieved by subtracting a baseline estimated using the 'backcor' function. A second-order polynomial with an asymmetric truncated quadratic cost function and a threshold of 0.1 was used for all spectra, except for measurements on carbon black, which required a third-order polynomial due to more intense fluorescence. In some cases, the constant term in the polynomial was adjusted to shift the polynomial up or down before subtraction to preserve peak integrity. Finally, the spectra were normalized by rescaling them to a 0–100 range using MATLAB's 'rescale' function.

2.4. Catalyst evaluation for RWGS reaction

The catalysts were tested in the RWGS reaction in a vertical fixed bed reactor. A total of 70 mg of the catalyst was placed on quartz wool in the middle of the reactor of 7 mm inner diameter. The catalytic tests were then performed at atmospheric pressure and at a H_2:CO_2 ratio of 2:1. The stability tests were performed at atmospheric pressure and at a H_2:CO_2 ratio of 3:1.We performed temperature screening tests between 100 °C and 600 °C using 100 mL/min total flow (84,714 mL/g/h) and stability tests for 250 h at 600 °C with the same total flow. The reactants and products were analysed using an online ABB AO2020 advanced optima process gas analyser, equipped with thermal conductivity and infrared detectors. The conversion and selectivity values were calculated using the following equations:

$$CO_2\text{conversion}(\%) = \frac{[CO_2]_{in} - [CO_2]_{out}}{[CO_2]_{in}} \text{x}100$$

$$CO\ \text{selectivity}(\%) = \frac{[CO]_{out}}{[CO_2]_{in} - [CO_2]_{out}} \text{x}100$$

2.5. Computational calculations

The Density functional Theory (DFT) calculations were performed in Indian Institute of Technology Roorkee using Quantum Espresso 7.2 software. The electronic structures were visualized using a plane wave basis set and the Perdew-Burke-Ernzerhof (PBE) exchange correlation with Projector-Augmented-Wave (PAW) Pseudopotentials. NEB calculations were performed to find the energy barrier and the activation for the RWGS reaction over the catalyst. The creation and visualization of the structures and the calculation of angles and bond length of the optimized structure were performed using VESTA, Burai, and Xcrysden. The free energy change for each step was separately calculated using computational hydrogen electrode model. Details are given in the supporting information.

3. Results and discussion

Boron nano sheets were synthesized by reacting $NaBH_4$ and HCOOK at molar ratios ranging from 1:1–3:1, followed by stepwise heating to 600 °C under inert atmosphere (Fig. 1). At 3:1 and 2:1 ratio, reduced boron nanosheets (BH) were obtained, designated as BH_NaK_3:1 and BH_NaK_2:1, respectively (Fig. 1-Route a, Scheme S1). Conversely, it was surprising to find that a 1:1 ratio resulted in the formation of oxidized boron nanosheet (BO) designated as BO_NaK. (Please note that the materials are designated in the following manner: Lattice type_Alkali metals of borohydride and of formate_ratio of borohydride to formate. Since BO is produced exclusively with 1:1 ratio, ratio is omitted from its designation). Further, the materials were characterized by using different techniques such as Powder X-ray diffraction (PXRD), X-ray Photoelectron Spectroscopy (XPS), Fourier Transform Infrared Spectroscopy (FTIR), Raman spectroscopy, Atomic Force Microscopy (AFM), and High-Resolution Transmission Electron Microscopy (HRTEM), Scanning Transmission Electron Microscopy-Energy-Dispersive X-ray

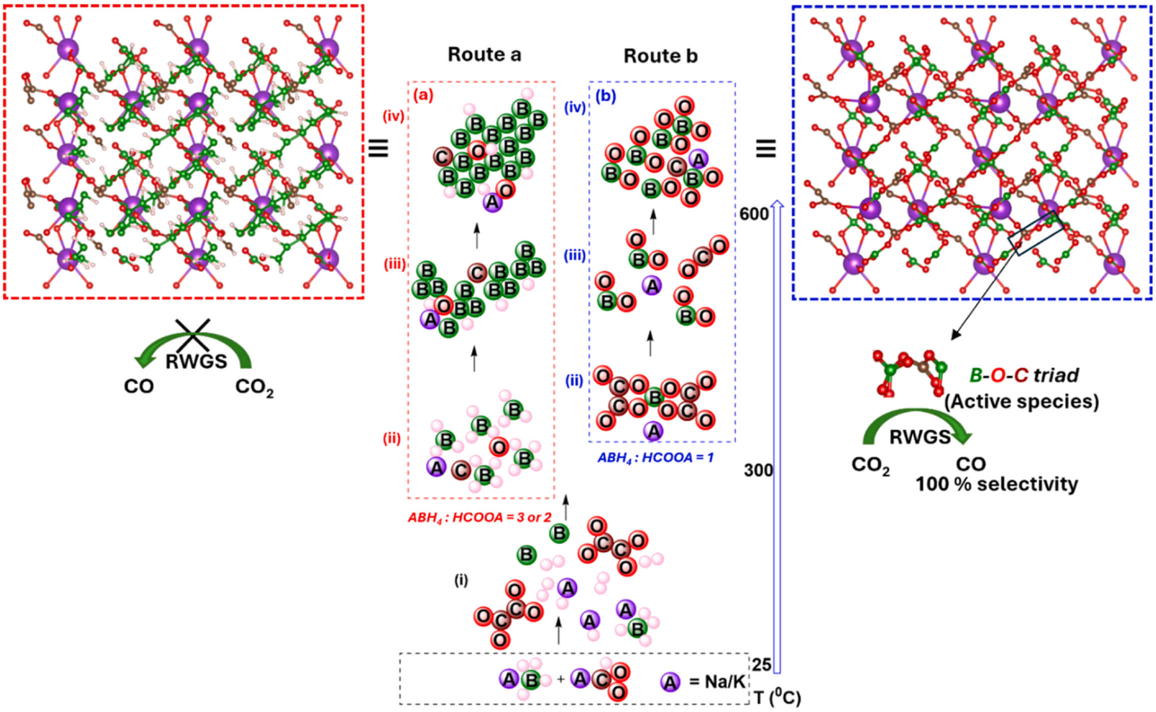

Fig. 1. Schematic representation for the formation of (a) BHs and (b) BOs; and their catalytic performance towards the RWGS reaction. The formation of final lattice depends on the relative abundance of oxalate ions, produced from the decomposition of formate, at the initial synthesis stage (i). The abundant presence of oxalate ions at 1:1 ratio (route b) results in a chelating effect with the unstable boron intermediates generated from the decomposition of borohydride, leading to oxaloborates in stage (ii). At temperatures above 320 °C, oxaloborates decompose into borate anions (BO_2^-), stage (iii). Further rapid increase in temperature to 600 °C converts borate species into BO sheets (iv). However, lack of sufficient oxalate ions (route a) at higher ABH_4:HCOOA ratios led to oxygen deficient and hydrogen rich BH lattices.

Spectroscopy (STEM-EDS). Density Functional Theory (DFT) calculations were also performed to gain a better insight into the structure and catalytic activity.

The reduced BH lattice is formed via alkali-metal-assisted self-catalyzed growth (Fig. 1a, Fig. S1a) [13]. During this process, HCOOK decomposition generates a reducing environment that stabilizes reactive boron intermediates formed from the thermal decomposition of $NaBH_4$; enabling BH lattice formation. On the other hand, the unprecedented formation of a B-O rich lattice upon changing the molar ratio of $NaBH_4$ and HCOOK to 1 is accounted for by the following rationale: At a ratio of 1, the concentration of oxalate ions ($C_2O_4^{2-}$) in the reaction (stage (i), Fig. 1), produced from the decomposition of HCOOK, surpasses that observed at ratios of 2 and 3. These oxalate ions serve as excellent chelating agents [18,19]. Therefore, the reaction is likely to be driven by the abundant presence and chelating characteristics of oxalate ions [19]. It is assumed that the oxalate ions further interact with the unstable boron intermediates generated by the decomposition of borohydride, resulting in the formation of oxaloborates (stage (ii), Fig. 1b) [20]. Subsequently, oxaloborates, when subject to temperatures above 320 °C, decompose into borate anions (BO_2^-) as shown in stage (iii), Fig. 1b, [21]. A further rapid increase in temperature to 600 °C facilitates the transformation of BO_2^- species into BO sheets (Fig. 1b, Scheme S1b) [22, 23]. DFT calculations validated the feasibility BO synthesis from stage (iii) via the proposed mechanism. The four different base structures with h p k values of (100), (110), (101), and (111) were optimized (Fig. S15), followed by the optimization of parameters such as kinetic energy cut-off for wavefunctions (ecutwfc), the kinetic energy cut-off for charge density and potential (ecutrho), thresholds of force and energy, and convergence criteria. The results revealed that the formation of the BO lattice from borate anions requires a minimal 1.87 eV energy whereas the dissociation of B-O bond from the lattice of BO demands 3.41 eV energy. This suggested that, while high temperatures are essential during the synthesis process, the resulting BO lattice exhibits stability afterwards.

After washing and subsequent workup, the materials were tested for the RWGS reaction in a vertically fixed bed reactor. We began by testing the catalytic activity of the materials across temperatures between 100 °C and 600 °C, at atmospheric pressure and at a H_2/CO_2 ratio of 2. The results demonstrated that BO_NaK catalyzes the RWGS reaction efficiently whereas BH sheets do not (Fig. 2a). Surprisingly, the BH sheets remained inactive in the RWGS reaction, even with the H_2/CO_2 ratio raised to 4. We also tested the catalytic activity of BH samples synthesized at a slow heating rate (1–10 °C/min), to determine whether there is a correlation between the material's crystallinity and their catalytic performance [13]. However, no BH sheets exhibited any catalytic activity. BO_NaK, on the other hand, initiated its catalytic activity at 500 °C and demonstrated equilibrium conversion at 600 °C, achieved under a high space velocity of 85714 mL/g/h and H_2/CO_2 ratio of 2.

To gain deeper understanding of this unprecedented activity, we opted to conduct a comprehensive study of the BO system. Therefore, we pursued the synthesis of BO_KK (by reacting KBH_4 and HCOOK) and BO_NaNa (by reacting $NaBH_4$ and HCOONa) (Fig. 1 and Scheme S1). The reactants were utilized in a 1:1 molar ratio and underwent the same sequential heating procedure as mentioned in Scheme S1b to produce BO_KK and BO_NaNa. Further, both BO_KK and BO_NaNa were tested in RWGS reaction, under similar conditions and feed gas flow with a H_2/CO_2 ratio of 2. The results revealed that BO_KK acts as a superior catalyst compared to BO_NaK, whereas BO_NaNa exhibited no activity in the RWGS reaction (Fig. 2a). The catalytic activity of BO_KK began at 500 °C, demonstrating a significantly higher CO_2 conversion of 16 % compared to BO_NaK (5 %) and attained equilibrium conversion at a lower temperature (550 °C) than BO_NaK. Both BO_NaK and BO_KK exhibited 100 % CO selectivity throughout the entire temperature range in which it was operational, even at a high H_2/CO_2 ratio of 4, where methanation is highly favored (Fig. 2b). The long-term stability of the active catalysts was examined at a space velocity of 85714 mL/g/h and H_2/CO_2 ratio of 3. The BO catalysts exhibited excellent long-term stability and 100 % CO selectivity at 600 °C making it an excellent candidate for moderate-high temperature RWGS catalyst (Fig. 2c). Comparison of stability, CO selectivity and kinetic performance of BOs with existing renowned catalysts are shown in Fig. 3a,b. To the best of our knowledge, the only metal-free (*no metal is present either as an active species or in support*) RWGS catalyst reported in literature is nitrogen doped graphene quantum dots [24]. However, they exhibited much lower CO selectivity and CO productivity compared to our BO catalysts at a comparatively high pressure (10 bar). Notably, the widely used Cu-Zn-Al catalyst suffers a 70 % activity loss within 15 h, while BO_KK showed no deactivation after 250 h at 600 °C (Fig. 2c, Fig. 3a, Table S1). Additionally, the kinetic performance of BO_KK and BO_NaK is superior or equivalent to most of the noble/transition metal/metal oxide-based catalysts (Fig. 3b, Table S2); although it is not as high as that of cubic α-Mo_2C and β-Mo_2C catalysts [11,25–42].

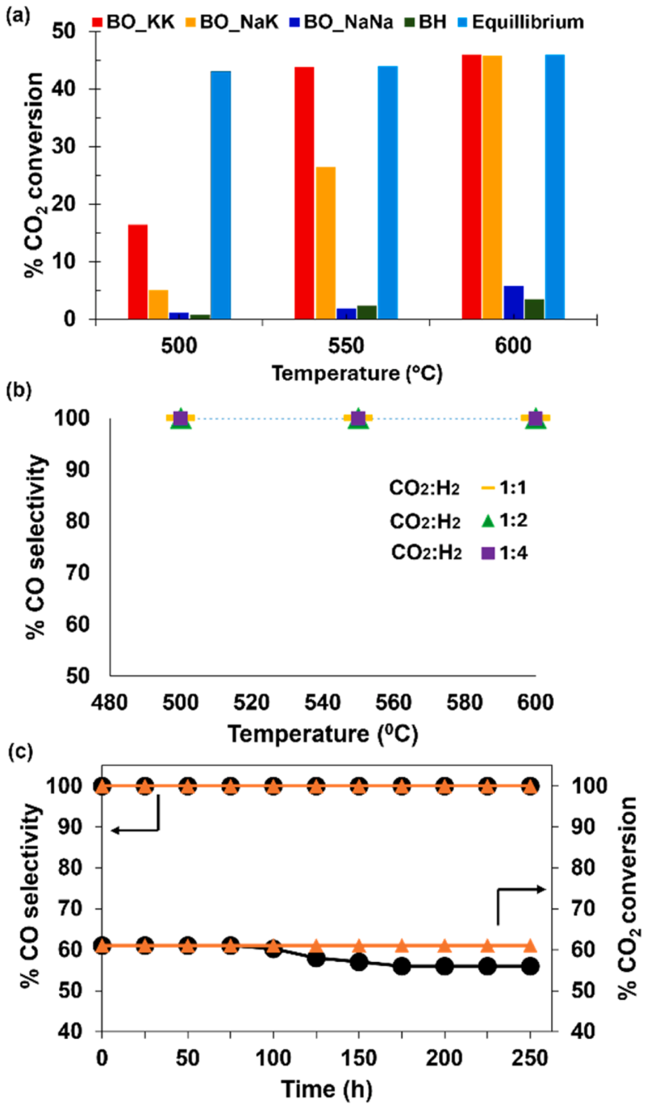

Fig. 2. Catalyst performance of BHs and BOs in RWGS reaction. (a) %CO_2 conversion at space velocity 85714 mL/g/h, when H_2/CO_2 ratio is 2, at 1 bar pressure, in the temperature range between 500 °C and 600 °C; (b) CO selectivity of BO_KK at a space velocity of 85714 mL/g/h, with different H_2/CO_2 ratios, at 1 bar pressure, in the temperature range between 500 °C and 600 °C; (c) The 250 h stability test of BO_KK (orange) and BO_NaK (black) at a space velocity of 85714 mL/g/h, with a H_2/CO_2 ratio 3, at 1 bar pressure and 600 °C.

The overall outcome of the RWGS reaction was not entirely anticipated, especially the complete inactivity of BHs and BO_NaNa. To fully

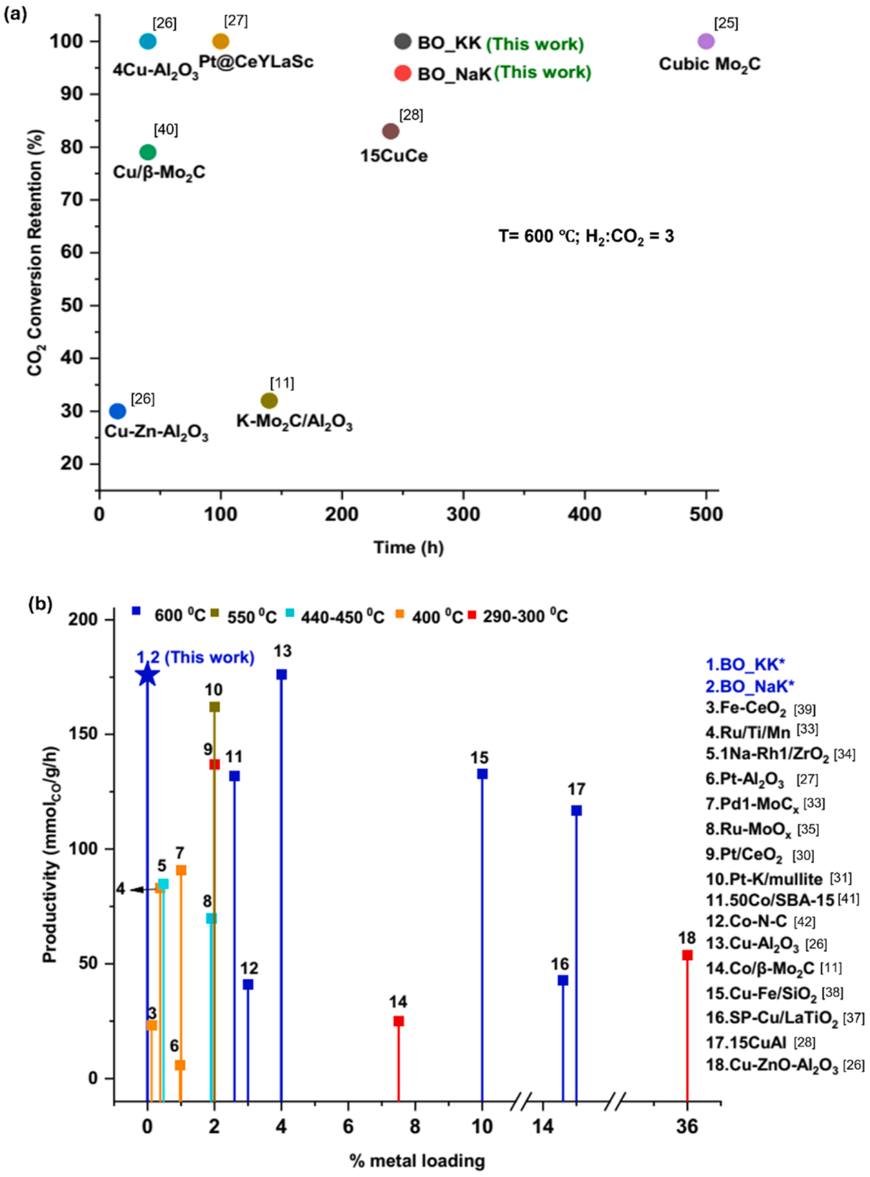

Fig. 3. Comparison of the RWGS performance by BO sheets with state-of-the-art catalysts. (a) %CO$_2$ conversion retention (% of the original CO$_2$ conversion remained after a given time on stream) of BO catalysts (this work) and reported catalysts at 600 °C when H$_2$:CO$_2$ is 3:1; (b) CO productivity of BO catalysts (this work) and state of the art catalysts.

comprehend the differences in catalytic activity, detailed structural characterization was conducted on both pristine and spent BHs and BOs. FTIR, Raman, and XPS analyses unambiguously revealed that BH sheets consist of a hydrogenated B-B lattice with both terminal and bridgind hydrogens (B-H and B-H-B), along with B-C and B-O bonds (Fig. S1a-d) [13,43]. Further, the TEM and AFM analyses illustrated ultrathin BH sheets with a thickness of ~4 nm, while both XRD and TEM confirmed their amorphous nature (Fig. S1e, f, Fig. S3). It is probable that the amorphous nature of BH sheets arose from the accelerated rate of heating (25 °C/min) employed during its synthesis. A comprehensive characterization of all the BH sheets and starting materials is provided in the supporting information (Fig. S1- S3).

On the other hand, the spectral (FTIR, XPS and Raman) features of thin BO sheets (with lateral size between 1.5 and 3.5 μm for BO_NaK and 0.3–1.0 μm for BO_KK; and thickness as low as 0.94 nm for BO_NaK and 2.0 nm for BO_KK; Fig. S4, S5) differed greatly from those of BH sheets indicative of a lattice enriched with B-O bonds, oxygen containing organics and hydroxyl functionalities (Fig. 4a, Fig. S6-S8) [44–47]. Analysis of the Raman spectra (Fig. S6a) for BOs revealed the presence of pentaborate groups in the lattice, characterized by a prominent peak at 770 cm^{-1}, alongside various B-O deformations that have been previously reported in the literature (Fig. S6a) [44,48]. The bands at 1343 cm^{-1} and 1571 cm^{-1} in the Raman spectrum of both BOs and BHs (Fig. S6b) belong to the carbonaceous material formed during the synthesis.

The spectral analysis of the ‘spent BO’ samples recorded after the RWGS reaction revealed valuable insights into the discrepancies in activity. The FTIR spectra of spent BO_KK and BO_NaK revealed a new sharp band at 1425 cm^{-1} together with additional bands of small-medium intensity in the 800–1450 cm^{-1} region (Fig. 4e). Additionally, the C═O, C-O, B-O, and O-H bands showed shifts and reduced intensity relative to the corresponding pristine samples. These spectral changes are consistent with the formation of boron-oxy-carbon linkages (B-O-C) on the surface of BO_KK and BO_NaK during the reaction [47]. However, BO_NaNa_spent showed no 1425 cm^{-1} band characteristic of B-O-C linkages, with spectral features in this region remaining unchanged from pristine BO_NaNa. Their XPS analysis provided further validation for this observation (Fig. 4, Fig. S7, S8) [49,50]. For instance, the B 1s

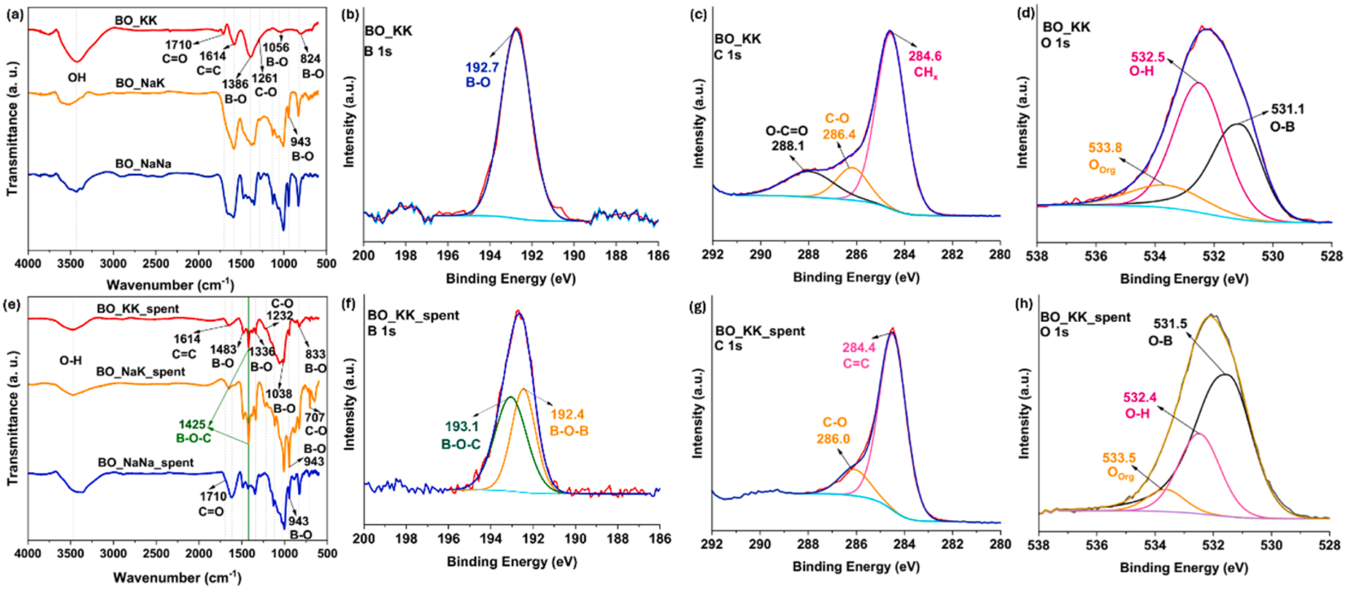

Fig. 4. Spectral characterization of BOs. (a) FTIR of pristine BOs; (b-d) XPS of BO_KK; (e) FTIR of spent BOs; (f-h) XPS of BO_KK_spent.

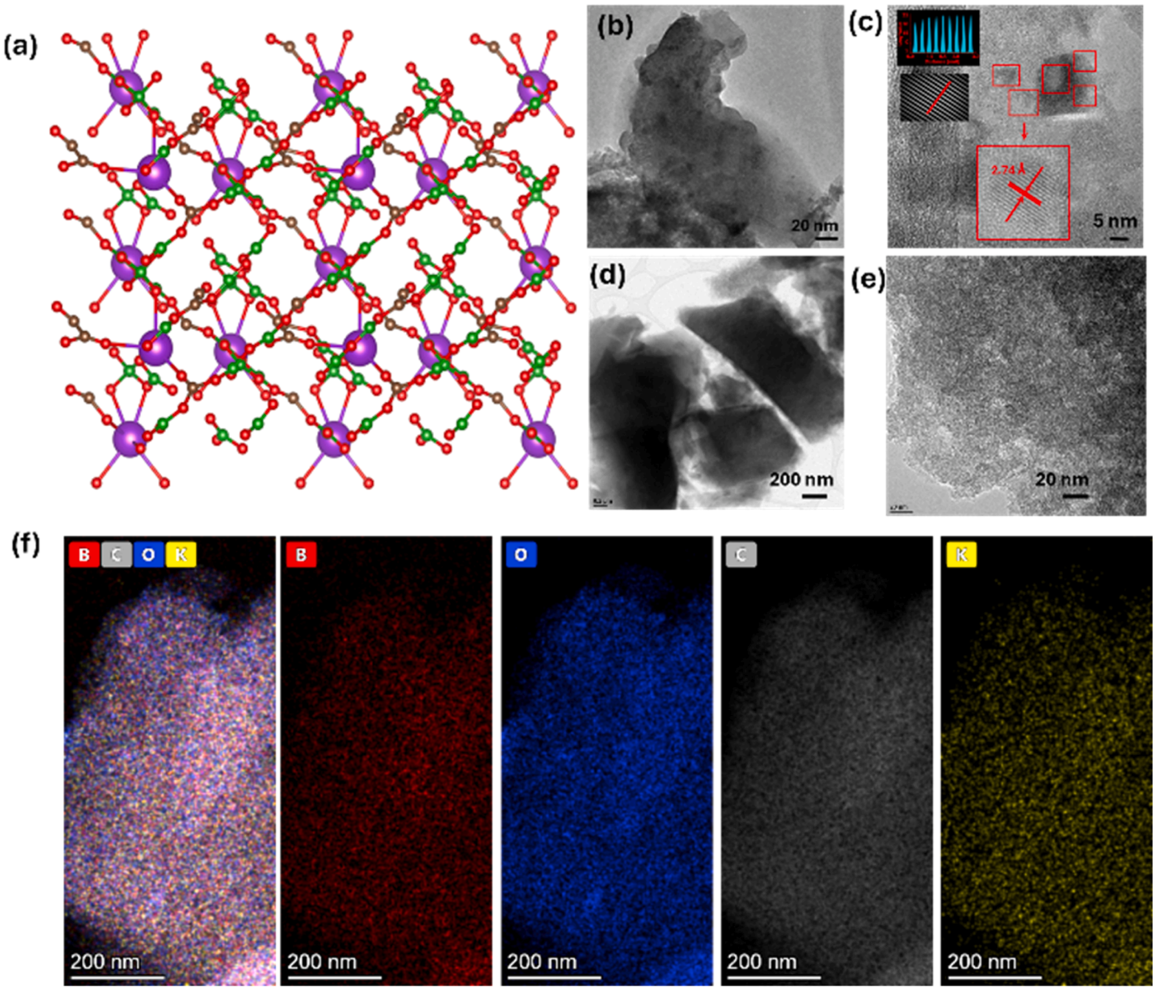

Fig. 5. (a) Front and side views of optimized structure of BO_KK@450 (Boron in green, Oxygen in red, Carbon in brown and Potassium in purple); (b, c) HRTEM images of BOKK@450; (d, e) HRTEM image of BO_KK_spent; (f) STEM-EDS analysis of BO_KK@450.

spectrum of spent BO_KK and BO_NaK deconvoluted into B-O-B and B-O-C components, in contrast to the single sharp B 1s peak of the pristine catalysts. Comparison of the O 1s and C 1s spectra of pristine and spent catalysts further confirmed ‘B-O-C’ formation, accompanied by the loss of oxygenated organics and surface hydroxyl groups. C 1s XPS indicated the presence of an ultrathin CH_x adsorbate layer on the pristine BOs, which was below the detection limit of FTIR. Upon reaction, this layer was removed, as evidenced by a shift in the C 1s peak from 284.8 to 284.4 eV, revealing the underlying $C{=}C$ framework (Fig. 4c). Notably, the XPS spectra of spent BO_NaNa showed no evidence of the B-O-C component (Fig. S8). This was intriguing and implied that the stable surface ‘B-O-C triad’ could potentially be the active species for the RWGS reaction.

We initially hypothesized that the formation of ‘B-O-C triad’ occurs when the catalyst is subjected to the feed gases (CO_2 and or H_2). However, it was found to generate abundantly when the pristine BO catalysts were subjected to temperatures above 450 °C (BO@450) in an inert atmosphere (Fig. S9). FTIR spectra of BO_KK@450 and BO_NaK@450 closely matched those of the corresponding spent samples, confirming the formation of stable B-O-C species under these conditions; whereas that of BO_NaNa@450 remained unchanged. These observations suggested that potassium (K) present in the catalyst plays a crucial role in promoting the formation of the active ‘B-O-C triad’, which subsequently catalyzes the RWGS reaction (500 ℃ onwards); thereby explaining the inactivity of BO_NaNa. BO_NaCs (synthesised via the thermal decomposition of $NaBH_4$ and $CsCO_3$) was inactive in the RWGS reaction, which further proved that the active species forms only when K is present. The concentration potassium in BO_KK@450 determined by ICP-OES was found to be 6 μg/L.

DFT calculations provided further insight into the structure of the active species in BO catalysts. Out of the four lattice structures simulated with h p k values (1 0 0), (1 1 0), (1 0 1) and (1 1 1), the optimum structure of BO_KK@450 (active BO_KK) revealed that the (1 0 0) configuration represents the optimal structure (Fig. 5a, Fig. S15, S16a-d). The calculated lattice spacing of 2.75 Å (Fig. S17), obtained from DFT calculations aligned well with the observed ones (2.74 Å) in the HR-TEM image of BO_KK@450 (Fig. 5b,c, Fig. S10). Both the HRTEM and STEM-EDS images of BO_KK@450 and the BO_KK_spent after long term reaction clearly showed that the catalyst retained its structural integrity after long term reaction (Fig. 5b-f, Fig. S10-S12). Further, EDS analysis confirmed the absence of any metallic impurities in BO_KK@450, that could contribute to the observed RWGS activity (Fig. S11b).

After successfully characterizing the catalyst and studying its activity towards the RWGS reaction, combined experimental and theoretical efforts were undertaken to unravel the role of each element (B, O, C and K) in the observed activity/inactivity and selectivity of the materials. It is already evident that K has a significant role in the formation of the active ‘B-O-C triad’. Additionally, K is also recognized for its role as a promoter that enhances CO_2 adsorption. The electron-donating effect of K can elevate the number of basic sites present on the catalyst surface, which in turn boosts catalytic activity [11,12]. Simultaneously it limits the hydrogen adsorption and prevents the methanation of CO_2 and increases the CO-selectivity. Both the CO_2-TPD and H_2-TPD results agreed with this argument (Fig. S13). The CO_2-TPD profile of BOKK@450 displayed a higher density of moderate basic sites than BONaK@450, which are ideal for CO_2 chemisorption. Overall, the synergy of stronger CO_2 adsorption and better H_2 activation makes BOKK@450 more effective for promoting the RWGS reaction under the studied conditions.

Once we had established the function of K in the catalytic process, the next step was to confirm that the proposed B-O-C triad is the true active species. Considering this, the first step was to exclude the possibility that carbonaceous material formed from the thermal decomposition of HCOOK could serve as the active species. To do so, HCOOK was thermally treated at 600 °C using the same program and workup (Scheme S1). Raman spectra identified the resulting black solid as graphitic carbon (Figure S6b). The material was inactive towards the RWGS reaction, indicating that carbon alone or in combination with K is insufficient to drive the reaction. These findings exclude the presence of catalytically relevant K_2CO_3 in the material (which could have formed from the decomposition of HCOOK) and therefore rule out a carbonate mediated RWGS pathway [51,52]. Given that dispersed Na_2CO_3 is also known to catalyze the RWGS reaction, the lack of activity observed for BO_NaNa further undermines alkali-metal carbonate-driven activity in the BO system [51].

We further ruled out boron as the sole active species by verifying that materials obtained from the thermal decomposition of $NaBH_4$ or KBH_4 alone demonstrate no RWGS activity. Additionally, the inactivity of BHs, despite containing the same elements (B, C, K and O) indicates that an ‘oxygen-enriched lattice’ is required to generate the active sites and achieve catalytic performance. Consistent with this, introducing C and K into boron nitride (BN) or boron carbide (BC) by decomposing HCOOK in their presence produced materials that were also inactive in RWGS reaction. Together, these results demonstrated that an oxygen-enriched boron lattice is essential for RWGS activity in the BO catalysts. This further distinguishes the BO catalysts from alkali metal carbonate catalysts that can function even on non-oxide supports such as granular activated carbon [51]. Based on these distinctions, we propose that oxidized boron frameworks represent a new class of RWGS catalysts, mechanistically distinct from seemingly similar systems reported in the literature.

We further probed the adsorption of CO_2 and H_2 over BO_KK@450, via projected density of states (PDOS) calculations (Fig. S18-S22). The adsorption of only CO_2 did not produce any significant change in PDOS values (Fig. S19), whereas the adsorption of H_2 did change the PDOS values (Fig. S20). Maximum PDOS values of B, C and O increased by 10 %, whereas that of K decreased by 15 %, which showed that the adsorption of H_2 is greatly affected by the presence of K in the catalyst lattice. The interaction of adsorbed CO_2 and H_2 changed the maximum PDOS values of B, C, O and K atoms by 20 %. The net 20 % change in maximum PDOS values signified the change in electronic properties of CO_2 and H_2 in adsorbed state as compared to the molecular phase. The overlapping curves of B, C, O and K in Fig. S22 confirmed adsorption of CO_2 and H_2 over catalyst surface. The electropositive nature of K increased the adsorption tendency of CO_2 and H_2 over the active BO_KK surface, in agreement with the TPD results.

The RWGS mechanism over BO_KK@450 was investigated using diffuse reflectance infrared Fourier transform (DRIFTS) spectroscopy. Utilizing an in-situ DRIFT set up, we observed the formation of CO with the band at 2143 cm^{-1} implying the dissociation of CO_2 to CO(g) (Fig. S14). However, despite repeated attempts, we were unable to detect any additional surface species [53]. Likewise, there was no indication of an alkali metal carbonate-catalyzed mechanism, which would be expected to procced via a formate intermediate [51–53]. These results suggest a reaction pathway involving the dissociative adsorption of CO_2 on the surface of BO-based catalysts [53]. Therefore, further insights into the reaction mechanism were obtained through DFT calculations. The configuration and energy profiles of each step and reaction mechanism are shown in Fig. 6a,b and Fig. S23. The adsorption energies of −0.090 eV and −0.019 eV respectively for CO_2 and H_2 revealed the energetic favorability of the adsorption over BO_KK@450. The relative free energy change (ΔG) of adsorption of reactants (CO_2* and H_2*) was observed to be −1.31 eV. Both reactants adsorb over the nearest B atoms associated with the ‘B-O-C triad’ on the active BO_KK lattice. O and H atoms present towards molecular phase ($\Delta G = -0.12$ eV) interact to form a carboxyl intermediate (HOCO*). Subsequently, HOCO* dissociated into CO* and O* with a ΔG of −0.18 eV. The process of CO desorption encountered an energy barrier of 1.11 eV, along with an additional 0.28 eV necessary for the formation of H* and OH*. This intermediate step is followed by the released CO (in molecular phase) and adsorbed H_2O (H_2O*), with ΔG equal to 0.78 eV. Finally, H_2O undergoes spontaneous desorption characterized with a ΔG of −0.51 eV.

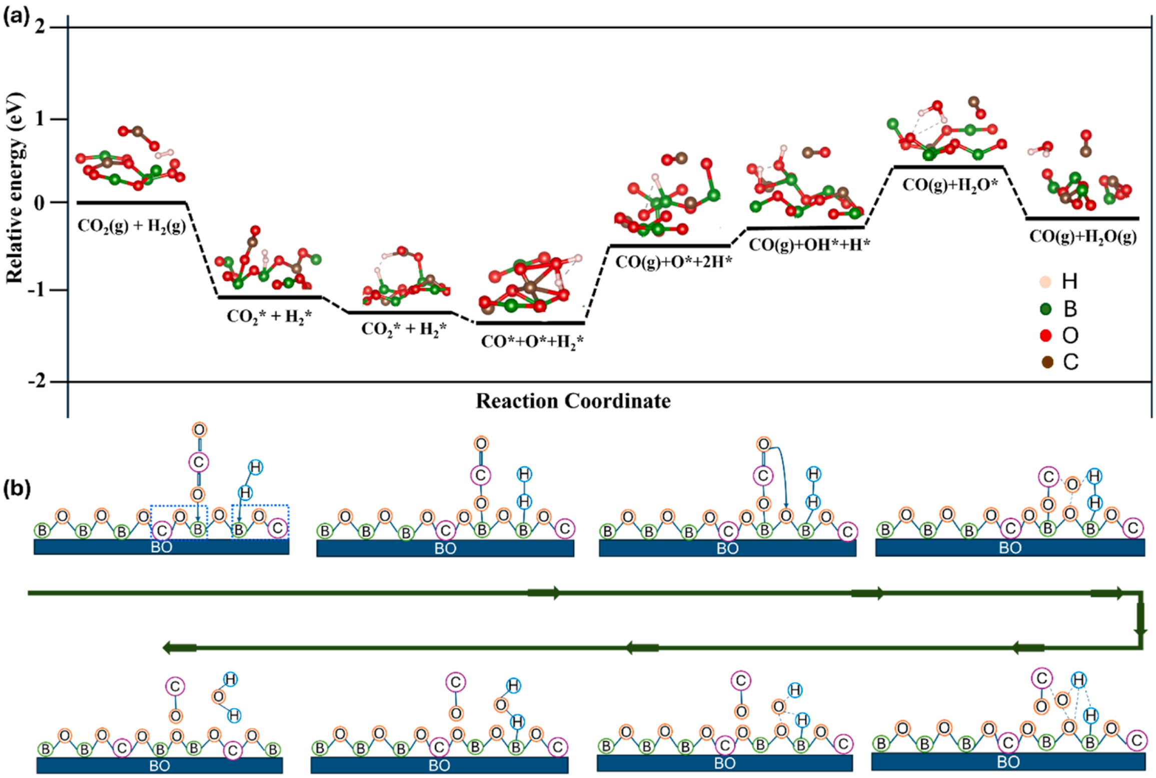

Fig. 6. Reaction mechanism for the RWGS reaction over BO_KK@450 via DFT calculations. (a) Relative free energy for all the steps of the RWGS. The images in Fig. 6a are from different orientations, shown to best illustrate the interactions. Additional views of the various steps are provided in Fig. S23; (b) Reaction mechanism.

Different mechanisms were examined to confirm that the above represents the most plausible pathway. The calculations performed via the Langmuir-Hinshelwood mechanism, considering adsorption on the boron atoms that do not belong to the B-O-C triad, presented an activation energy of 8.27 eV for the RWGS reaction. Similarly, the reaction mechanism in which the adsorption of H_2 took place over C atom of active surface, followed by interaction with neighboring adsorbed CO_2 molecule over B atom, a high activation energy of 13.007 eV was observed. This indicates that while the B-O-C triad is essential for activation, direct H_2-C interaction suppresses activity, highlighting the need to limit C content in the catalyst lattice. In comparison, the Mars-van Krevelen mechanism yielded an activation energy of 8.48 eV for the same interaction. The high activation energies suggested that these mechanisms are not feasible for the RWGS process over the BO_KK@450 catalyst. It is also important to note that the energy of adsorption for CO_2 and H_2 on the BH sheet was found to be high (7.34 eV and 5.62 eV respectively), indicating that additional energy is necessary for the adsorption. On a broader perspective, this study highlights the importance of tailored active sites and controlled surface chemistry for CO_2 conversion reactions, aligning with previous studies [54–56].

4. Conclusion

In summary, we report a facile, cost-effective, and scalable synthesis strategy based on rational element selection, yielding metal-free boron-oxy-carbide catalysts for the RWGS reaction. This approach is broadly applicable and enables the design of tunable catalysts for diverse reactions. To the best of our knowledge, this work presents the first truly metal-free RWGS catalyst achieving high performance under ambient pressure. 'B-O-C triad' present within the catalyst's lattice enabled effective activation of both CO_2 and H_2 via dissociative HOCO pathway. The catalysts exhibited remarkable thermal stability, resistance to coking, complete CO selectivity and long-term stability. This provides significant benefits compared to traditional metal-based catalysts, making them ideal candidates for future industrial applications. Although the boron-oxy-carbide catalysts did not exhibit state-of-the-art performance at low temperatures, they reveal a paradigm shift in heterogeneous catalysis, where activity arises from tunable molecular and electronic design rather than metal centres. This offers substantial opportunities for enhancing the catalyst efficiency, with detailed mechanistic and performance investigations currently underway.

CRediT authorship contribution statement

Rajamohanan Sobhana Anju: Writing – original draft, Methodology, Investigation, Conceptualization. **Pankaj Kumar:** Writing – original draft, Methodology, Investigation. **Dhanaji R. Naikwadi:** Writing – review & editing, Methodology, Investigation. **Merel C. Konings:** Methodology, Investigation. **Pascal G. Stam:** Methodology, Investigation. **Freek Ariese:** Writing – review & editing, Supervision, Methodology, Investigation. **Bettina Baumgartner:** Writing – review & editing, Methodology, Investigation. **Atul Bansode:** Writing – review & editing, Supervision, Methodology, Investigation. **Fengshou Yu:** Methodology, Investigation. **Erdni D. Batyrev:** Writing – review & editing, Methodology, Investigation. **Paula Oulego:** Methodology, Investigation. **Vimal Chandra Srivastava:** Writing – review & editing, Supervision, Methodology, Investigation, Software, Resources. **N. Raveendran Shiju:** Writing – review & editing, Supervision, Software, Resources, Project administration, Methodology, Conceptualization.

Declaration of Competing Interest

The authors declare that they have no known competing financial interests or personal relationships that could have appeared to influence the work reported in this paper.

Acknowledgment

RSA and NRS would like to thank the European Commission for a Marie Skłodowska-Curie Actions Postdoctoral Fellowship (Grant agreement number 101105834–2DBoroCat). B.B. acknowledges funding by the Dutch Research Council (NWO) under the grant number VI. Veni.222.253. PO would like to thank the Asturian Agency for Science, Business Competitiveness and Innovation (SEKUENS) for financial support through the project SEK-25-GRU-GIC-24–010. PK acknowledges the National Supercomputing Mission (NSM) for providing computing resources of 'PARAM Ganga' at the Indian Institute of Technology Roorkee, which is implemented by C-DAC and supported by the Ministry of Electronics and Information Technology (MEIT) and Department of Science and Technology (DST), Government of India.

Appendix A. Supporting information

Supplementary data associated with this article can be found in the online version at doi:10.1016/j.apcatb.2025.126153.

Data Availability

The data are provided in the manuscript and in the supporting information.

References

[1] G. Xu, C. Cai, W. Zhao, Y. Liu, T. Wang, WIREs Comput. Mol. Sci. 13 (2023) e1654, https://doi.org/10.1002/wcms.1654.

[2] M. Ronda-Lloret, L. Yang, M. Hammerton, V.S. Marakatti, M. Tromp, Z. Sofer, A. Sepúlveda-Escribano, E.V. Ramos-Fernandez, J.J. Delgado, G. Rothenberg, T. Ramirez Reina, N.R. Shiju, ACS Sustain. Chem. Eng. 9 (2021) 4957–4966, https://doi.org/10.1021/acssuschemeng.0c07881.

[3] T. Mathew, S. Saju, S.N. Raveendran, in: *Engineering Solutions for CO_2 Conversion*, Wiley, 2021, pp. 281–316.

[4] X. Sun, J. Yu, H. Zada, Y. Han, L. Zhang, H. Chen, W. Yin, J. Sun, Nat. Chem. (2024), https://doi.org/10.1038/s41557-024-01628-4.

[5] S. Sengupta, A. Jha, P. Shende, R. Maskara, A.K. Das, J. Environ. Chem. Eng. 7 (2019) 102911, https://doi.org/10.1016/j.jece.2019.102911.

[6] P. Ranjan, J.M. Lee, P. Kumar, A. Vinu, Adv. Mater. 32 (2020) 2000531, https://doi.org/10.1002/adma.202000531.

[7] R.S. Anju, N.R. Shiju, Mater. Today 88 (2025) 393–414, https://doi.org/10.1016/j.mattod.2025.03.028.

[8] S. Mohanty, D. Panda, A. Dash, S.S. Kumar, R.R. Padhi, S. Guhathakurata, S. Mallik, J. Electron. Mater. 52 (2023) 4434–4454, https://doi.org/10.1007/s11664-023-10367-0.

[9] T. Goto, S.I. Ito, S.L. Shinde, R. Ishibiki, Y. Hikita, I. Matsuda, I. Hamada, H. Hosono, T. Kondo, Commun. Chem. 5 (2022) 118, https://doi.org/10.1038/s42004-022-00739-8.

[10] E.S. Erakulan, R. Thapa, Appl. Surf. Sci. 574 (2022) 151613, https://doi.org/10.1016/j.apsusc.2021.151613.

[11] J. Xu, X. Gong, R. Hu, Z.W. Liu, Z.T. Liu, Mol. Catal. 516 (2021) 111954, https://doi.org/10.1016/j.mcat.2021.111954.

[12] J. Gándara-Loe, Q. Zhang, J.J. Villora-Picó, A. Sepúlveda-Escribano, L. Pastor-Pérez, T. Ramirez Reina, Energy Fuels 36 (2022) 6362–6373, https://doi.org/10.1021/acs.energyfuels.2c00784.

[13] C. Hou, G. Tai, J. Hao, L. Sheng, B. Liu, Z. Wu, Angew. Chem. Int. Ed. 59 (2020) 10819–10825, https://doi.org/10.1002/anie.202001045.

[14] T. Meisel, Z. Halmos, K. Seybold, E. Punór, J. Therm. Anal. 7 (1975) 73–80, https://doi.org/10.1007/BF01911627.

[15] Y. Gao, S. Jaenicke, G.-K. Chuah, Appl. Catal. A Gen. 484 (2014) 51–58, https://doi.org/10.1016/j.apcata.2014.07.010.

[16] H. Wiener, B. Zaidman, Y. Sasson, Int. J. Hydrog. Energy (1989) 365–370, https://doi.org/10.1016/0360-3199(89)90166-3.

[17] M. Baidossi, A.V. Joshi, S. Mukhopadhyay, Y. Sasson, Synth. Commun. 34 (2004) 643–650, https://doi.org/10.1081/SCC-120027711.

[18] A. G. M. M. B. F. Albert Cotton, Advanced Inorganic Chemistry, in: Advanced Inorganic Chemistry, Wiley-Interscience, 1999, pp. 484–487.

[19] D.V. Uríková, G. Kampitakis, I. Císařová, A. Alemayehu, M. Kloda, D. Zákutná, K. Lang, J. Demel, V. Tyrpekl, Inorg. Chem. 64 (2025) 3686–3695, https://doi.org/10.1021/acs.inorgchem.4c04293.

[20] E. Bessler, J. Weidlein, Z. Naturforsch. B 37 (1982) 1020–1025, https://doi.org/10.1515/znb-1982-0813.

[21] P.Y. Zavalij, S. Yang, M.S. Whittingham, Acta Cryst. 59 (2003) 753–759, https://doi.org/10.1107/S0108767303009713.

[22] Y. Wang, L. Xing, X. Tang, X. Li, W. Li, B. Li, W. Huang, H. Zhou, X. Li, RSC Adv. 4 (2014) 33301–33306, https://doi.org/10.1039/C4RA03018D.

[23] N.I. Leonyuk, V.V. Maltsev, E.A. Volkova, Molecules 25 (2020) 2450, https://doi.org/10.3390/molecules25102450.

[24] J. Wu, C. Wen, X. Zou, J. Jimenez, J. Sun, Y. Xia, M.T. Fonseca Rodrigues, S. Vinod, J. Zhong, N. Chopra, I.N. Odeh, G. Ding, J. Lauterbach, P.M. Ajayan, ACS Catal. 7 (2017) 4497–4503, https://doi.org/10.1021/acscatal.7b00729.

[25] M.A. Khoshooei, X. Wang, G. Vitale, F. Formalík, K.O. Kirlikovali, R.Q. Snurr, P. Pereira-Almao, O.K. Farha, Science 384 (2024) 540–546, https://doi.org/10.1126/science.adl1260.

[26] A.M. Bahmanpour, F. Héroguel, M. Kıllç, C.J. Baranowski, L. Artiglia, U. Röthlisberger, J.S. Luterbacher, O. Kröcher, ACS Catal. 9 (2019) 6243–6251, https://doi.org/10.1021/acscatal.9b01822.

[27] X. Liu, S. Huang, D. Yuan, S. Li, L. Ma, L. Gao, Z. Li, Y. Wang, Y. Li, J. Ye, Inorg. Chem. Front (2025) 4041–4047, https://doi.org/10.1039/D5QI00274E.

[28] H.X. Liu, S.Q. Li, W.W. Wang, W.Z. Yu, W.J. Zhang, C. Ma, C.J. Jia, Nat. Commun. 13 (2022) 867, https://doi.org/10.1038/s41467-022-28476-5.

[29] F.G. Baddour, E.J. Roberts, A.T. To, L. Wang, S.E. Habas, D.A. Ruddy, N. M. Bedford, J.A. Schaidle, R.L. Brutchey, N. Malmstadt, J. Am. Chem. Soc. 142 (2020) 1010–1019, https://doi.org/10.1021/jacs.9b11238.

[30] A. Goguet, F. Meunier, J. Breen, R. Burch, M. Petch, A. Faurghenciu, J. Catal. 226 (2004) 382–392, https://doi.org/10.1016/j.jcat.2004.06.011.

[31] B. Liang, H. Duan, X. Su, X. Chen, Y. Huang, X. Chen, J.J. Delgado, T. Zhang, Catal. Today 281 (2017) 319–326, https://doi.org/10.1016/j.cattod.2016.02.051.

[32] H. Kang, L. Zhu, S. Li, S. Yu, Y. Niu, B. Zhang, W. Chu, X. Liu, S. Perathoner, G. Centi, Y. Liu, Nat. Catal. 6 (2023) 1062–1072, https://doi.org/10.1038/s41929-023-01040-0.

[33] Y. Ma, Y. Ren, Y. Zhou, W. Liu, W. Baaziz, O. Ersen, C. Pham-Huu, M. Greiner, W. Chu, A. Wang, T. Zhang, Y. Liu, Angew. Chem. 132 (2020) 21797–22180, https://doi.org/10.1002/ange.202007707.

[34] S. Li, Y. Xu, H. Wang, B. Teng, Q. Liu, Q. Li, L. Xu, X. Liu, J. Lu, Angew. Chem. Int. Ed. 62 (2023) e202218167, https://doi.org/10.1002/anie.202218167.

[35] H. Xin, L. Lin, R. Li, D. Li, T. Song, R. Mu, Q. Fu, X. Bao, J. Am. Chem. Soc. 144 (2022) 4874–4882, https://doi.org/10.1021/jacs.1c12603.

[36] C. Chen, W. Cheng, S. Lin, Catal. Lett. 68 (2000) 45–48, https://doi.org/10.1023/A:1019071117449.

[37] J. Yu, X. Sun, X. Tong, J. Zhang, J. Li, S. Li, Y. Liu, N. Tsubaki, T. Abe, J. Sun, Nat. Commun. 12 (2021) 7209, https://doi.org/10.1038/s41467-021-27557-1.

[38] C. Chen, Appl. Catal. A Gen. 257 (2004) 97–106, https://doi.org/10.1016/S0926-860X(03)00637-9.

[39] B. Dai, G. Zhou, S. Ge, H. Xie, Z. Jiao, G. Zhang, K. Xiong, Can. J. Chem. Eng. 95 (2017) 634–642, https://doi.org/10.1002/cjce.22730.

[40] X. Zhang, X. Zhu, L. Lin, S. Yao, M. Zhang, X. Liu, X. Wang, Y.-W. Li, C. Shi, D. Ma, ACS Catal. 7 (2017) 912–918, https://doi.org/10.1021/acscatal.6b02991.

[41] H. Liang, B. Zhang, P. Gao, X. Yu, X. Liu, X. Yang, H. Wu, L. Zhai, S. Zhao, G. Wang, A.P. van Bavel, Y. Qin, Chem. Catal. 2 (2022) 610–621, https://doi.org/10.1016/j.checat.2022.01.020.

[42] Y. Li, Z. Zhao, W. Lu, H. Zhu, F. Sun, B. Mei, Z. Jiang, Y. Lyu, X. Chen, L. Guo, T. Wu, X. Ma, Y. Meng, Y. Ding, Appl. Catal. B 324 (2023) 122298, https://doi.org/10.1016/j.apcatb.2022.122298.

[43] H. Nishino, T. Fujita, N.T. Cuong, S. Tominaka, M. Miyauchi, S. Iimura, A. Hirata, N. Umezawa, S. Okada, E. Nishibori, A. Fujino, T. Fujimori, S.I. Ito, J. Nakamura, H. Hosono, T. Kondo, J. Am. Chem. Soc. 139 (2017) 13761–13769, https://doi.org/10.1021/jacs.7b06153.

[44] T. Kambe, R. Hosono, S. Imaoka, A. Kuzume, K. Yamamoto, J. Am. Chem. Soc. 141 (2019) 12984–12988, https://doi.org/10.1021/jacs.9b06110.

[45] Q. Gu, H. Lin, C. Si, Z. Wang, A. Wang, F. Liu, B. Li, B. Yang, ACS Nano 18 (2024) 30574–30583, https://doi.org/10.1021/acsnano.4c09002.

[46] Y. Wu, Y. Zhao, Q. Yuan, H. Sun, A. Wang, K. Sun, G.I.N. Waterhouse, Z. Wang, J. Wu, J. Jiang, M. Fan, Nat. Commun. 15 (2024) 10843, https://doi.org/10.1038/s41467-024-55071-7.

[47] X. Liu, X. Chen, D.J. Singh, R.A. Stern, J. Wu, S. Petitgirard, C.R. Bina, S. D. Jacobsen, Proc. Natl. Acad. Sci. U. S. A. 116 (2019) 7703–7711, https://doi.org/10.1073/pnas.1821612116.

[48] D. Maniu, T. Iliescu, I. Ardelean, S. Cinta-Pinzaru, N. Tarcea, W. Kiefer, J. Mol. Struct. 651-653 (2003) 485–488, https://doi.org/10.1016/S0022-2860(03)00129-7.

[49] S. Mondal, A.K. Banthia, J. Eur. Ceram. Soc. 25 (2005) 287–291, https://doi.org/10.1016/j.jeurceramsoc.2004.08.011.

[50] G. Socrates, Infrared and Raman Characteristic Group Frequencies, Wiley, Chichester, 2004.

[51] C.S. Li, A.D. Frankhouser, M.W. Kanan, Cell Rep. Phys. Sci. 3 (2022) 101021, https://doi.org/10.1016/j.xcrp.2022.101021.

[52] K.N. Tamakuwala, R.P. Kennedy, C.S. Li, B. Mutz, P. Boller, S.R. Bare, M.W. Kanan, JACS Au 5 (2025) 1083, https://doi.org/10.1021/jacsau.5c00127.

[53] L.F. Bobadilla, J.L. Santos, S. Ivanova, J.A. Odriozola, A. Urakawa, ACS Catal. 8 (2018) 7455–7467, https://doi.org/10.1021/acscatal.8b02121.

[54] S. Saju, S. Rajendran, U. Oztas, S.C. Ruiz, T.R. Reina, B. Ghosh, S.P. Sree, R. Meena, G. Li, L.F. Bobadilla, C.P. Vinod, T. Mathew, N.R. Shiju, Towards improved activity and stability in RWGS reaction: Dispersed copper in mesoporous alumina matrix as a strategy for enhanced performance, Chem. Eng. J. 525 (2025) 169863.

[55] E.V. Ramos-Fernandez, N.R. Shiju, G. Rothenberg, Understanding the solar-driven reduction of CO_2 on doped ceria, RSC Adv. 4 (2014) 16456–16463.

[56] M. Ronda-Lloret, V.S. Marakatti, W.G. Sloof, J.J. Delgado, A. Sepúlveda-Escribano, E.V. Ramos-Fernandez, G. Rothenberg, N.R. Shiju, Butane Dry Reforming Catalyzed by Cobalt Oxide Supported on Ti2AlC MAX Phase, ChemSusChem 13 (2020) 6401–6408.